

A New Room-Temperature Quantum Emitter in High-Quality Hexagonal Boron Nitride.

Brian Shevitski^{1,2,3,4}, S. Matt Gilbert^{1,2,3}, Christopher T. Chen⁴, Christoph Kastl^{4,5}, Edward S. Barnard⁴, Ed Wong⁴, Kenji Watanabe⁶, Takashi Tanaguchi⁶, Alex Zettl^{1,2,3*}, and Shaul Aloni^{4*}

¹Department of Physics, University of California at Berkeley, Berkeley, CA 94720, U.S.A.

²Materials Sciences Division, Lawrence Berkeley National Laboratory, Berkeley, CA 94720, U.S.A.

³Kavli NanoEnergy Sciences Institute at the University of California at Berkeley and the Lawrence Berkeley National Laboratory, Berkeley, CA 94729, U.S.A.

⁴The Molecular Foundry, Lawrence Berkeley National Laboratory, Berkeley, CA 94720, U.S.A.

⁵Walter-Schottky-Institute and Physik Department, Technical University of Munich, Garching, 85748, Germany.

⁶Advanced Materials Laboratory, National Institute for Materials Science, 1-1 Namiki, Tsukuba, 305-0044, Japan

*To whom correspondence should be addressed: azettl@berkeley.edu, saloni@lbl.gov

Abstract

Light emitters in wide band gap semiconductors are of great fundamental interest and have potential as optically addressable qubits. Here we describe the discovery of a new quantum emitter in high-quality hexagonal boron nitride (h-BN) with a sharp emission line at 435 nm. The emitters are activated and deactivated by electron beam irradiation and have the spectral and temporal characteristics of single-photon emitters (SPEs) weakly coupled to lattice vibrations. The emitters are conspicuously absent from commercially available h-BN and are only present in ultra-high-quality h-BN grown using a special high-pressure method. This suggests that these emitters originate from impurities or related defects specific to this unique synthetic route. We propose a charged defect state as the origin of this new SPE.

Introduction

Single photon emitters (SPEs) are a likely component of next-generation information technologies, especially quantum cryptography^{1,2} and information processing^{3–5}. SPEs embedded in solid state systems are particularly significant for widespread adoption of these emerging technologies as they offer a promising route toward scalable deployment of new integrated quantum circuits. The diamond nitrogen-vacancy (NV) center has been the leading candidate for solid-state SPE applications because it can easily be manipulated and readout at room temperature using existing optical methods^{6,7}. Due to the technical difficulty of synthesizing and fabricating diamond-based devices, greater attention has been placed on finding new solid-state SPE systems^{8,9} with particular emphasis placed on 2D material systems, especially sp^2 -bonded hexagonal boron nitride (h-BN))^{10–14}.

h-BN or “white graphite” has been of great interest to the nanoscience community over the last several decades, in part because it is isostructural to graphite and forms many of the same types of nanostructures as sp^2 -bonded carbon, but with different electronic and thermodynamic properties^{15–19}. h-BN is especially important to the expanding study of 2D materials because it is atomically flat, inert, and electrically insulating, making it an ideal substrate for testing new physics in low-dimensional materials²⁰. Recently it has been shown that the local structure of h-BN can be controlled via electron irradiation^{21,22} and synthetic methods²³, allowing for additional material control.

In this communication we report the discovery of a new quantum photon emitter in high-quality h-BN, activated and characterized by an electron beam. We show that these emitters are highly localized, are spectrally pure, and have an emission signature indicative of weak lattice

coupling at room temperature. These properties make the new SPE promising for future applications in quantum information science.

Experimental

Ultra-high-quality h-BN crystals used in this study (generally accepted as the best h-BN available) are synthesized using a Ba-B-N solvent precursor at high temperature and high pressure at the National Institute for Materials Science (NIMS) by Watanabe and Tanaguchi²⁴. We refer to this material throughout the text as NIMS-BN. Millimeter size crystallites are mechanically exfoliated and transferred silicon substrates with a few nm thick native oxide layer. Samples of commercially available h-BN are similarly exfoliated and transferred, and then annealed (see Methods) before characterization.

We use CL in the scanning electron microscope (SEM) to activate and characterize light emission from the h-BN. CL measurements are performed using a home-built SEM CL system shown in Fig. 1. The system is built around a Zeiss Gemini Supra 55 VP-SEM operated at accelerating voltages between 2-10 keV with beam currents in the 100-1500 pA range. Light emission from the sample is collected by a parabolic mirror and directed down an optical path for characterization. Synchronous data from SEM and optical channels are acquired using the Molecular Foundry ScopeFoundry software²⁵. All experiments are conducted at room temperature.

As the electron beam is rastered across the sample, the spectral distribution of the light emission from each point of the scan can be recorded on a spectrometer resulting in a three-dimensional data set we refer to as a spectral image (SI). Alternatively, the light can be directed through a series of dichroic mirrors and bandpass filters to an array of photon counting point-detectors, resulting in

intensity images of well-defined wavelength bands. We refer to such data throughout the text as bandpass (BP) images.

Time-correlation of the emitted light can be measured by coupling to a Hanbury-Brown-Twiss (HBT) interferometer. The arrival times of photons at the detectors in both arms of the interferometer are recorded with 50 ps resolution and a coincidence histogram as a function of delay time between the two detectors is made. The raw coincidence histogram is then normalized by the number of coincidences at long delay times in the usual way. A background correction is performed using the signal to background ratio estimated independently for each measurement²⁶, resulting in a measurement of the second-order auto-correlation function ($g^{(2)}(\tau)$) of the emitted light.

All data analysis is performed using common open-source packages in the Python programming language. Multivariate statistical analysis (MVA) of hyperspectral images is carried out using the HyperSpy Python package²⁷.

Results

We first describe results from NIMS-BN. In order to activate and characterize individual emitters, we initially identify large (lateral size of 10-100 μm) flakes of h-BN using the raster scan images from the SEM electron detectors, shown in Figure 2(a). Optical and atomic force microscopy (AFM) observations of our samples indicate that the flakes generally have thicknesses of several hundred nanometers. Relevant spectral bands for BP imaging are determined by inspection of the average CL spectrum, shown in Figure 2(b), obtained by integrating spectra while continuously scanning a single flake. We isolate the primary spectral regions of interest (indicated by the vertical lines and shaded regions in Figure 2(b)): 280-409 nm (UV), 430-470 nm (Blue), and 485-735 nm (Vis) for BP imaging with appropriate dichroic and bandpass optics.

There are several striking features in each channel of the BP images. Fig. 2(c) shows the spatial distribution of the previously reported UV emitters in the h-BN flake^{5/3/2019 3:37:00 PM}. The emitters have a point-like character and are densely and uniformly distributed across the entire h-BN crystal, with enhanced emission along line-like features that are likely associated with extended line defects²⁸ or strain caused by a wrinkle or fold in the crystallite²⁹.

Fig. 2(e) shows very weak extended features in the Vis band (485-735 nm) as previously reported²⁸. These features are localized at grain-boundaries and dislocations within the h-BN crystal. No localized, point-like sources of light emission are observed within this band using CL BP imaging.

The bright, point-like features in the Blue BP image between 430-470 nm in Fig. 2(d) show the new quantum emitters in NIMS-BN, which are the focus of this study. They appear slightly larger and less dense compared to the UV emitters in the previous panel. Also present is the line-like feature from the UV band, as well as a very weak signal from extended features in the Vis band. The broad spectral character of these extended features results in residual intensity “leaking” into the Blue band.

We further characterize electron-stimulated light emission from NIMS-BN using hyperspectral CL imaging by collecting a CL spectrum from each pixel in a raster scan. To isolate the unique spectral signature of each type of emitter we perform a non-negative matrix factorization (NMF) decomposition³⁰ of the spectra in the SI into four components that visualize the main features present in the dataset. Figs. 3(a-f) show the results of the decomposition. Each image (also called the decomposition loading or decomposition weight) shows the relative abundance of each associated spectral component (also called the decomposition factor) below.

The vertical red lines in Figs. 3(a), 3(c), and 3(e) show the pass band used for BP imaging in Figs. 2(c), 2(d), and 2(e), respectively.

The first component (not shown) is a spatially uniform background that reflects dark counts, noise, and non-localized light emission. The component shown in Figs. 3(e) and 3(f) shows the light emission of extended line defects, as well as a small number of highly localized features with appreciable intensity that are consistent with previous photoluminescence (PL) studies^{10,11} of SPE in h-BN.

Fig. 3(a) shows a dense collection of point-like emitters, similar to the UV BP image in Fig. 2(b). The spectral features in the component in Fig. 3(b)) are characteristic of UV SPEs in h-BN, confirming that these emitters are the same as previous CL studies¹⁴.

The most striking feature, shown in Figs. 3(c) and 3(d), closely matches the spectral signature of a typical color center in a wide bandgap semiconductor^{10,12}, and clearly shows the nature of the new quantum emitters. This component is investigated further in Fig. 3(g) using multi-Gaussian fitting of the spectral component. Fitting reveals a series of peaks, decreasing in intensity and increasing in width with increasing wavelength. The signature is dominated by a sharp, well-defined zero phonon line (ZPL), centered at 436 nm (2.84 eV), followed by several phonon replicas at 443, 461, and 484 nm (2.80, 2.69, and 2.56 eV). There is also a small, broad, background component centered at 482 nm (2.57 eV). In contrast to the UV emission described above (where the phonon replicas have higher intensity than the ZPL), the relatively high intensity of the ZPL compared to the phonon replicas suggest that this emitter's coupling to the lattice is significantly weaker, a desirable quality for SPE applications. The density of emitters in Fig. 3(c) is higher than in the BP image in Fig. 2(c) and is related to the higher electron dose required for hyperspectral imaging, which will be discussed later.

Spectral information from the hyperspectral imaging can be used to perform time-correlation measurements of light from the blue emitters. A bandpass filter is selected that covers a large portion of the emission peak from Fig. 3(d) in order to measure the second-order autocorrelation function using HBT interferometry. Fig. 3(h) shows the result of this measurement from an ensemble of emitters. In stark contrast to $g_{PL}^{(2)}(\tau)$ measured using PL, $g_{CL}^{(2)}(\tau)$ exhibits a bunching peak as opposed to an anti-bunching dip. This behavior, which has been explored previously^{31–33}, is consistent with the quantum nature of the emitters and is attributed to simultaneous excitation of multiple color centers by the electron beam. In PL, the excitation energy is less than the band-gap of the material, resulting in the production of a single e-h pair per photon. In CL, the excitation energy is much higher than the band-gap of the material, resulting in the excitation of many e-h pairs. A semi-empirical relation predicts that approximately $N_{e-h} = E_0/3E_g$ e-h pairs are excited per incident electron^[34], where E_0 is the beam energy and E_g is the bandgap of h-BN. For $E_g = 6 \text{ eV}$ and $E_0 = 3 \text{ keV}$, $N_{e-h} = 111$.

Previous work³² has shown that lifetime measurements from the bunching peak are indicative of the lifetime of the defect state and in agreement with analogous PL measurements from the anti-bunching dip. An exponential fit to the time correlation data using $g^{(2)}(\tau) = 1 + a \times \exp(-|\tau|/\tau_{lifetime})$, with a and $\tau_{lifetime}$ as free parameters, gives a lifetime of $\tau_{lifetime} = 2.6 \text{ ns}$ and $g^{(2)}(0) = 1.27$. The lifetime is close in value to similar measurements of other single photon emitters in h-BN. The $g^{(2)}(0)$ value is quite low, but it has been shown that at high current, the bunching effect becomes washed out, resulting in a decreased apparent value of $g^{(2)}(0)$. Nevertheless, the presence of this peak is evidence that the newly discovered blue emitter is a single photon source.

There are two striking differences between the Blue quantum emitters in Fig. 2(d) and those in Fig. 3(c) that are associated with the higher electron dose required to acquire an SI compared to a BP image. First, the number and density of features is higher in the SI, indicating that we are creating new emitters by electron irradiation. Second, a variation in the shape of individual emitters appears. The emitters are round and symmetric in the BP image in Fig. 2(d), while many emitters appear to have a truncated shape in the SI component in Fig. 3(c). This truncation, discussed below, is associated with sudden activation or deactivation of while the beam is over an emitter. To further investigate this, we acquire a 2.5-hour time series of long scan time (262 seconds per image) BP images over a flake of h-BN. Each image corresponds to an exposed dose of $2.3 \times 10^7 \text{ e}^-/\text{\AA}^2$ per image, with a total exposed dose of $\sim 5.7 \times 10^8 \text{ e}^-/\text{\AA}^2$. Fig. 4 summarizes the results of this experiment. The top row shows the first (Fig. 4(a)), middle (Fig. 4(b)), and last (Fig. 4(c)) images from the time series at full spatial resolution. The colored boxes in the full resolution images indicate regions where we have cropped the data and displayed the entire time series in a 300 nm region around four emitters (Figs. 4(d-g)). Fig. 4(d) shows an emitter that is suddenly activated by the electron beam (indicated by the truncated disc shape of the emitter), remains in the emissive state for 5 frames, then suddenly blinks off for the remainder of the time series. Figs. 4(e-f) show emitters that blink on and off several times throughout the scan. Some of these blinking events appear as truncated discs, while some appear as the sudden appearance or disappearance of a bright spot from one frame to another. Fig. 4 illustrates that not only are the emitters activated and deactivated by the electron beam, but they also disappear and reappear in identical spatial locations (within the accuracy of our measurement).

We note that we have also attempted characterization of these emitters using PL. NIMS-BN samples on indexed Si substrates are seeded with emitters using the SEM, characterized using CL, and then transferred to a PL setup. No emission is observed using 532, 405, and 349 nm excitation. This fact, in conjunction with the blinking behavior observed under the electron beam, hints that the origin of this emission is associated with the charge state of a point defect, similar to SPE in other semiconductor systems^{35–37}. Furthermore, we note that the Blue 435 nm emission is not observed using PL or CL in any samples of commercial h-BN powder. This implies that the new emission is closely related to the unique synthetic origin of NIMS-BN.

Discussion

We consider possible mechanisms for the new SPE. We immediately rule out the direct creation of defects via knock-on damage and electron-beam-induced heating. The electron energy threshold for knock-on damage in h-BN is in the range of 70-80 keV^{38,39}, far greater than the 1-10 keV energy range of the SEM beam. Electron-beam-induced heating is unlikely due to the high thermal conductivity of h-BN along with the relatively low current of the electron beam. The change in temperature of the sample can be estimated assuming that energy from the electron beam is uniformly deposited in a sphere of radius R using $\Delta T = \frac{3IVf}{2\pi R\kappa}$, where I is the beam current, V is the beam accelerating voltage, f is the fraction of incident energy that is absorbed, and κ is the thermal conductivity of h-BN (600 W/m K)⁴⁰. Assuming that 100% of the incoming power is absorbed in a spherical interaction volume of radius $R = 30$ nm, a 2 keV electron beam with 1 nA of current causes a temperature increase of $\Delta T = 0.05$ K. This value would be even lower at increased accelerating voltage⁴¹ because the interaction size scales

approximately as $V^{1.75}$. Furthermore, due to the finite thickness of an h-BN flake, the fraction of energy from the beam deposited into the sample decreases at higher beam energies.

We propose that the origin of this new emitter is electron-beam-induced defect chemistry, outlined in Fig. 5. The as-synthesized NIMS-BN crystal has some initial concentration of vacancies and intercalated interstitials, illustrated in the cartoon in Fig. 5(a). Electron beam induced diffusion increases the mobility of the interstitials causing the impurities to diffuse towards the naturally occurring vacancies within the material, resulting in the interstitial and vacancy combining into a defect complex^{42,43} (Fig. 5(b)). The electron beam modifies the charge state of the defect causing it to change from a non-emissive to an emissive state, resulting in the production of photons (Fig. 5(c)). The charge state of the defect can also be modified in the opposite sense, resulting in emitters blinking on and off during a measurement. This change in charge state has two possible origins. One scenario is that incident beam and secondary electrons are captured by the defect complex, resulting in a negative charge state. Alternatively, the incident or secondary electrons ionize the defect, resulting in a positive charge state. Currently, neither possibility can be excluded suggesting future experiments and calculations.

We propose that this emission has not been previously observed in h-BN for several reasons. Past studies of SPEs in h-BN have typically not used NIMS-BN which has a unique synthetic origin, but rather commercially obtained h-BN. We surmise that the Ba-B-N solvent precursor used in the NIMS-BN synthesis could produce barium impurities in these samples, which would not be present in commercially obtained material synthesized using different growth precursors. Under the assumptions of our model, the new emission would not be observed in the absence of this unique impurity. PL studies of SPEs in h-BN that do use NIMS-BN have generally used a 532 nm laser excitation to probe the sample. This excitation energy is too low to probe a state

that emits at 435 nm. It is likely that the charge recombination dynamics in this regime are dominated by non-radiative transitions. It is possible that the 435 nm emission is only present using CL because of the large number of electron-hole pairs created per incident electron, as well as the high intensity of the electron probe. A final, more speculative reason that this emission has not been observed to date is the possibility that the particular defect complex responsible for the emission needs the high energy density of the electron beam in order to drive interstitial-vacancy recombination.

Conclusion

We have identified a new single photon emitter in high-quality hexagonal boron nitride using cathodoluminescence in the SEM. The emission is peaked at 435 nm and has spectral characteristics indicative of weak lattice coupling. Photon correlation measurements indicate that the defect state has a lifetime of 2.6 ns. The electron beam activates and deactivates emission from point defects in the crystal. We propose that this emission originates from a barium atom interstitial impurity forming a defect complex with a vacancy driven by the energy of the electron beam. The charge state of this defect is changed by the electron beam resulting in the emitters blinking on and off.

Methods

Sample Prep

High-Quality h-BN crystals are synthesized as reported previously²⁴. Bulk crystals are mechanically exfoliated using blue wafer dicing tape and transferred onto a p++ silicon substrate (0.001-100 Ω -cm) with a few nm thick native oxide layer. Commercially available h-BN powder

(Alfa Aesar 040608) samples are similarly exfoliated and transferred, and then annealed at 850 °C in argon at one Torr for one hour before characterization.

Cathodoluminescence Imaging

Our CL system is built around a Zeiss Gemini Supra 55 VP-SEM operated at accelerating voltages between 2-10 keV at beam currents in the 100-1500 pA range. Light emission from the sample is collected by a parabolic mirror and directed down an optical path for characterization. Synchronous data from SEM (secondary electron and in-lens detectors) and optical channels (photon counting point detectors and spectrometer) are acquired using the Molecular Foundry ScopeFoundry software²⁵.

Bandpass images are collected using three separate photon counting photomultiplier tubes (Hamamatsu H7360-01, Hamamatsu H7421-40, and Hamamatsu H7421-50).

Spectra are collected by coupling the emitted light into an optical fiber (Thorlabs FG200UEA) using a UV-enhanced Aluminum reflector. The fiber is coupled into the spectrometer (Princeton Instruments SP2300i) and spectra are recorded on a CCD camera (Andor 970-UVB). Spectra are not intensity corrected for the wavelength dependent efficiency of the spectrometer grating and CCD camera.

HBT Interferometry

Emitted light is first filtered using a 460/50 bandpass filter (Semrock). The filtered light is coupled to a 50/50 split fiber (Thorlabs TM105R5S1A) using a parabolic reflector. Each end of the split fiber is directed toward a Silicon avalanche photodiode (MPD PD-100-CTE-FC). A 470/100 bandpass filter (Semrock) is placed before each detector to reduce the Silicon afterglow effect.

Photon timing data are acquired using a PicoHarp 300 (PicoQuant) operated in T2 mode. Typical integration times range from 30 minutes to 2 hours. We monitor the total number of timing events recorded and stop integration between 10-100 million events. Background count rates are estimated by scanning a region and measuring the count rate far from an emitter. Typical count rate values are 1-3 kHz for the background and 10-20 kHz for the emitters. Coincidences from the raw timing data are placed into bins between 50-500 ps. The raw coincidence histogram is then normalized by the number of coincidences at long delay times in the usual way. Finally, the background correction is performed using the signal to background ratio estimated independently for each measurement.

Data Analysis

Image analysis, curve fitting, and multivariate decomposition are performed using open-source packages in the Python programming language. Time-series data are aligned and registered using template matching and cross-correlation. Spectral image MVA decomposition is performed using the HyperSpy package. In order to determine the number of components a singular value decomposition is first performed, and the number of decomposition components is chosen by inspecting the Scree plot. The final decomposition is performed using non-negative matrix factorization with a reduced number of final components.

Author Contributions

BS, SA, and AZ conceived the project. BS performed the electron microscopy and analyzed the data. BS, CTC, and CK performed optical characterization. SMG, KW, and TT prepared the samples. ESB and EW developed the hardware and software for CL characterization. BS, SA,

and AZ wrote the manuscript. SA and AZ supervised the project. All authors proofread the paper.

Competing Interests

The authors declare no competing interests.

Data Availability

The data presented in the manuscript and analysis code that were used in this study are available from the corresponding authors upon reasonable request.

Acknowledgements

This research was supported primarily by the Director, Office of Science, Office of Basic Energy Sciences, Materials Sciences and Engineering Division, of the U.S. Department of Energy under Contract No. DE-AC02-05-CH11231 within the sp²-Bonded Materials Program (KC-2207) which provided for design of the experiment, and collection and analysis of the CL data. Additional support was provided by the Director, Office of Science, Office of Basic Energy Sciences, Materials Sciences and Engineering Division, of the U.S. Department of Energy under Contract No. DE-AC02-05-CH11231 within the van der Waals Heterostructures Program (KCWF16), which provided for BN sample preparation. This work was also supported by the National Science Foundation under Grant # DMR-1807233 which provided for TEM structure and impurity characterization; and under Grant #1542741 which provided for development of optical instrumentation. Work at the Molecular Foundry was supported by the Office of Science, Office of Basic Energy Sciences, of the US Department of Energy under Contract No. DE-AC02-

05CH11231. SMG acknowledges support from a Kavli Energy Nano Sciences Institute Fellowship and an NSF Graduate Fellowship.

References

1. Lo, H.-K., Curty, M. & Tamaki, K. Secure quantum key distribution. *Nat. Photonics* **8**, 595–604 (2014).
2. Scarani, V. *et al.* The security of practical quantum key distribution. *Rev. Mod. Phys.* **81**, 1301–1350 (2009).
3. Kok, P. *et al.* Linear optical quantum computing with photonic qubits. *Rev. Mod. Phys.* **79**, 135–174 (2007).
4. O’Brien, J. L., Furusawa, A. & Vučković, J. Photonic quantum technologies. *Nat. Photonics* **3**, 687–695 (2009).
5. Northup, T. E. & Blatt, R. Quantum information transfer using photons. *Nat. Photonics* **8**, 356–363 (2014).
6. Kurtsiefer, C., Mayer, S., Zarda, P. & Weinfurter, H. Stable Solid-State Source of Single Photons. *Phys. Rev. Lett.* **85**, 290–293 (2000).
7. Neumann, P. *et al.* Multipartite Entanglement Among Single Spins in Diamond. *Science* **320**, 1326–1329 (2008).
8. Castelletto, S. *et al.* A silicon carbide room-temperature single-photon source. *Nat. Mater.* **13**, 151–156 (2014).
9. Morfa, A. J. *et al.* Single-Photon Emission and Quantum Characterization of Zinc Oxide Defects. *Nano Lett.* **12**, 949–954 (2012).
10. Martínez, L. J. *et al.* Efficient single photon emission from a high-purity hexagonal boron nitride crystal. *Phys. Rev. B* **94**, 121405 (2016).
11. Tran, T. T. *et al.* Quantum Emission from Defects in Single-Crystalline Hexagonal Boron Nitride. *Phys. Rev. Appl.* **5**, 034005 (2016).

12. Tran, T. T. *et al.* Robust Multicolor Single Photon Emission from Point Defects in Hexagonal Boron Nitride. *ACS Nano* **10**, 7331–7338 (2016).
13. Tran, T. T., Bray, K., Ford, M. J., Toth, M. & Aharonovich, I. Quantum emission from hexagonal boron nitride monolayers. *Nat. Nanotechnol.* **11**, 37–41 (2016).
14. Bourrellier, R. *et al.* Bright UV Single Photon Emission at Point Defects in h-BN. *Nano Lett.* **16**, 4317–4321 (2016).
15. Chopra, N. G. *et al.* Boron Nitride Nanotubes. *Science* **269**, 966–967 (1995).
16. Rubio, A., Corkill, J. L. & Cohen, M. L. Theory of graphitic boron nitride nanotubes. *Phys. Rev. B* **49**, 5081–5084 (1994).
17. Novoselov, K. S. *et al.* Two-dimensional atomic crystals. *Proc. Natl. Acad. Sci.* **102**, 10451–10453 (2005).
18. Nagashima, A., Tejima, N., Gamou, Y., Kawai, T. & Oshima, C. Electronic dispersion relations of monolayer hexagonal boron nitride formed on the Ni(111) surface. *Phys. Rev. B* **51**, 4606–4613 (1995).
19. Golberg, D., Bando, Y., Stéphan, O. & Kurashima, K. Octahedral boron nitride fullerenes formed by electron beam irradiation. *Appl. Phys. Lett.* **73**, 2441–2443 (1998).
20. Dean, C. R. *et al.* Boron nitride substrates for high-quality graphene electronics. *Nat. Nanotechnol.* **5**, 722–726 (2010).
21. Pham, T. *et al.* Formation and Dynamics of Electron-Irradiation-Induced Defects in Hexagonal Boron Nitride at Elevated Temperatures. *Nano Lett.* **16**, 7142–7147 (2016).
22. Gilbert, S. M. *et al.* Fabrication of Subnanometer-Precision Nanopores in Hexagonal Boron Nitride. *Sci. Rep.* **7**, 15096 (2017).

23. Gilbert, S. M. *et al.* Alternative stacking sequences in hexagonal boron nitride. *2D Mater.* **6**, 021006 (2019).
24. Taniguchi, T. & Watanabe, K. Synthesis of high-purity boron nitride single crystals under high pressure by using Ba–BN solvent. *J. Cryst. Growth* **303**, 525–529 (2007).
25. Durham, D. B., Ogletree, D. F. & Barnard, E. S. Scanning Auger spectromicroscopy using the ScopeFoundry software platform. *Surf. Interface Anal.* **50**, 1174–1179 (2018).
26. Brouri, R., Beveratos, A., Poizat, J.-P. & Grangier, P. Photon antibunching in the fluorescence of individual color centers in diamond. *Opt. Lett.* **25**, 1294–1296 (2000).
27. Francisco de la Peña *et al.* *hyperspy/hyperspy: HyperSpy 1.3.1*. (Zenodo, 2018). doi:10.5281/zenodo.1221347
28. Jaffrennou, P. *et al.* Origin of the excitonic recombinations in hexagonal boron nitride by spatially resolved cathodoluminescence spectroscopy. *J. Appl. Phys.* **102**, 116102 (2007).
29. Proscia, N. V. *et al.* [arxiv]]Near-deterministic activation of room-temperature quantum emitters in hexagonal boron nitride. *Optica* **5**, 1128–1134 (2018).
30. Arngren, M., Schmidt, M. N. & Larsen, J. Unmixing of Hyperspectral Images using Bayesian Non-negative Matrix Factorization with Volume Prior. *J. Signal Process. Syst.* **65**, 479–496 (2011).
31. Feldman, M. A. *et al.* Colossal photon bunching in quasiparticle-mediated nanodiamond cathodoluminescence. *Phys. Rev. B* **97**, 081404 (2018).
32. Meuret, S. *et al.* Photon Bunching in Cathodoluminescence. *Phys. Rev. Lett.* **114**, 197401 (2015).
33. Meuret, S. *et al.* Photon bunching reveals single-electron cathodoluminescence excitation efficiency in InGaN quantum wells. *Phys. Rev. B* **96**, (2017).

34. Klein, C. A. Bandgap Dependence and Related Features of Radiation Ionization Energies in Semiconductors. *J. Appl. Phys.* **39**, 2029–2038 (1968).
35. Hauf, M. V. *et al.* Chemical control of the charge state of nitrogen-vacancy centers in diamond. *Phys. Rev. B* **83**, 081304 (2011).
36. Siyushev, P. *et al.* Optically Controlled Switching of the Charge State of a Single Nitrogen-Vacancy Center in Diamond at Cryogenic Temperatures. *Phys. Rev. Lett.* **110**, 167402 (2013).
37. Grotz, B. *et al.* Charge state manipulation of qubits in diamond. *Nat. Commun.* **3**, 729 (2012).
38. Kotakoski, J., Jin, C. H., Lehtinen, O., Suenaga, K. & Krashennnikov, A. V. Electron knock-on damage in hexagonal boron nitride monolayers. *Phys. Rev. B* **82**, 113404 (2010).
39. Zobelli, A., Gloter, A., Ewels, C. P., Seifert, G. & Colliex, C. Electron knock-on cross section of carbon and boron nitride nanotubes. *Phys. Rev. B* **75**, 245402 (2007).
40. Reimer, L. *Scanning Electron Microscopy: Physics of Image Formation and Microanalysis*. **45**, (2013).
41. Donolato, C. An analytical model of SEM and STEM charge collection images of dislocations in thin semiconductor layers. II. EBIC images of dislocations. *Phys. Status Solidi A* **66**, 445–454 (1981).
42. Dyck, O., Kim, S., Kalinin, S. V. & Jesse, S. Placing single atoms in graphene with a scanning transmission electron microscope. *Appl. Phys. Lett.* **111**, 113104 (2017).
43. Hudak, B. M. *et al.* Directed Atom-by-Atom Assembly of Dopants in Silicon. *ACS Nano* **12**, 5873–5879 (2018).

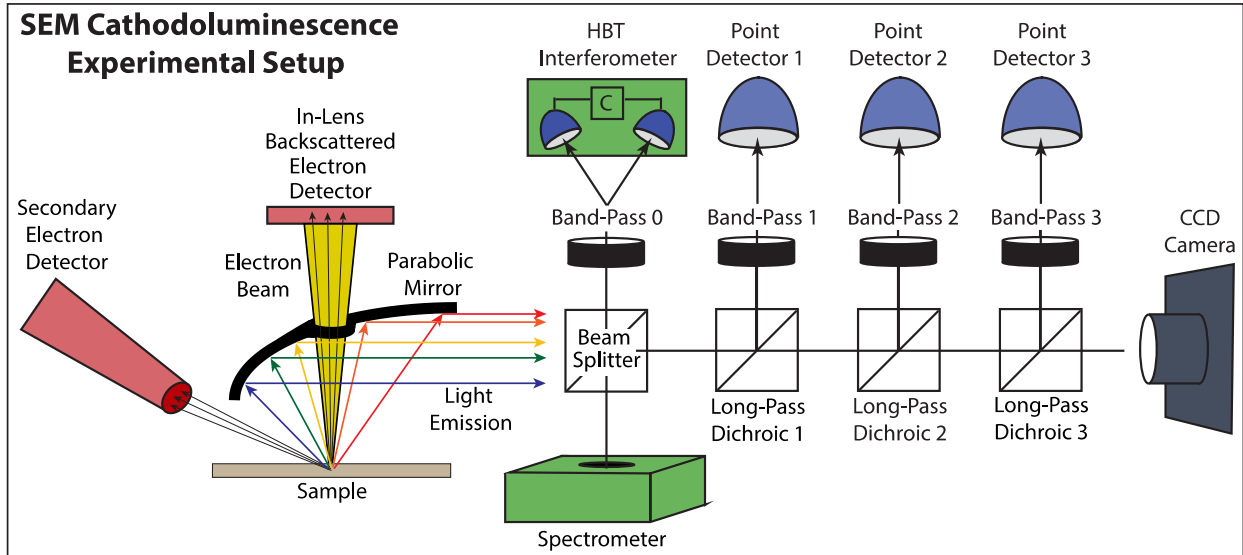


Figure 1: Experimental setup for measuring single photon emission from cathodoluminescence (CL) in the scanning electron microscope (SEM). The electron beam excites the sample and causes it to fluoresce. The resulting light is then used for hyperspectral imaging by a spectrometer (slow acquisition, low signal to noise, high spectral resolution) and point detectors (fast acquisition, high signal to noise, low spectral resolution). A Hanbury-Brown Twiss (HBT) interferometer is used to measure the second order coherence function ($g^{(2)}(\tau)$) of quantum emitters.

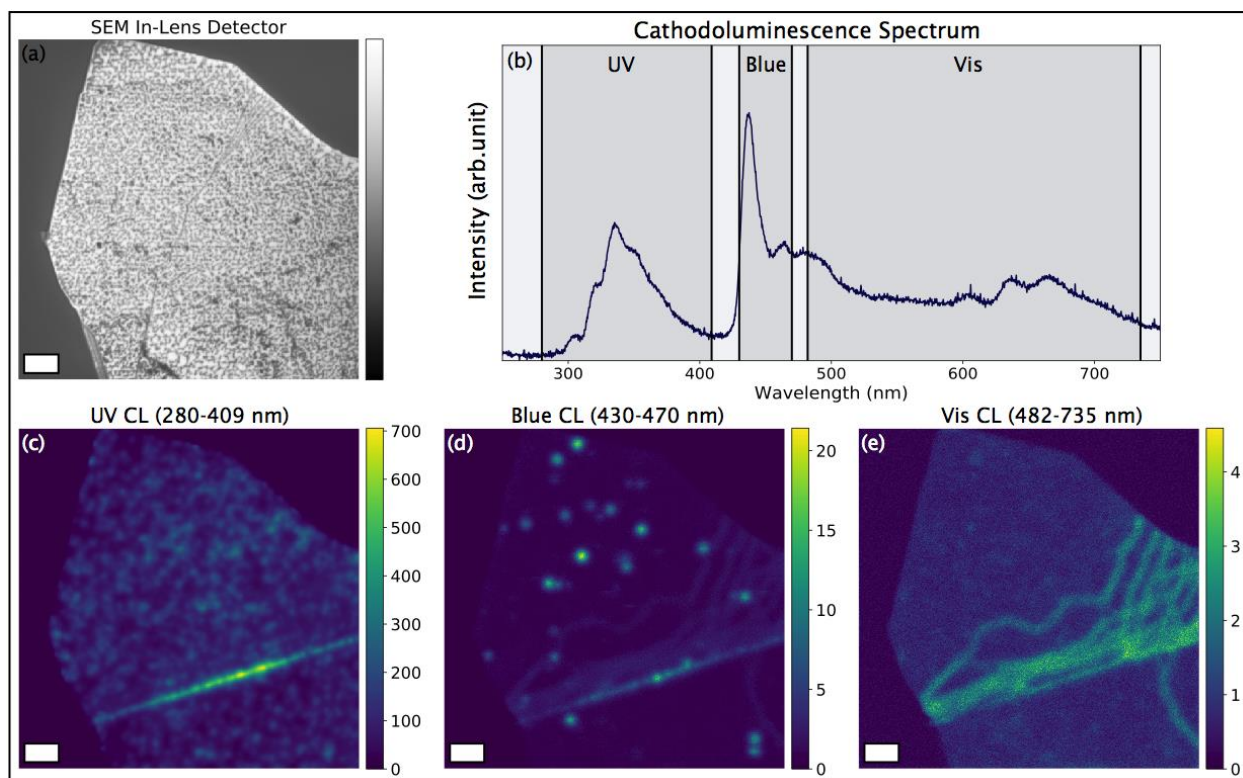


Figure 2: Overview of light emission from h-BN. An SEM image of a flake of h-BN is shown in (a), scale bar is 1 μm . Panel (b) shows the mean Cathodoluminescence (CL) response from the sample, with the three main spectral bands of interest indicated by vertical lines and shaded regions. Panels (c-e) show the light emission from the flake in each of these 3 spectral bands (wavelength range listed above each image, intensity scale in counts/second). Panel (c) shows UV light emission from a high density of point-like emitters as well as bright emission from a large line-like feature. The intensity in the Blue band arises mostly from the new point-like emitters, shown in Panel (d). Panel (e) shows the spatial distribution of intensity from the green to red region of the spectrum (Vis). Emission in this band arises mostly from extended defects in the crystal.

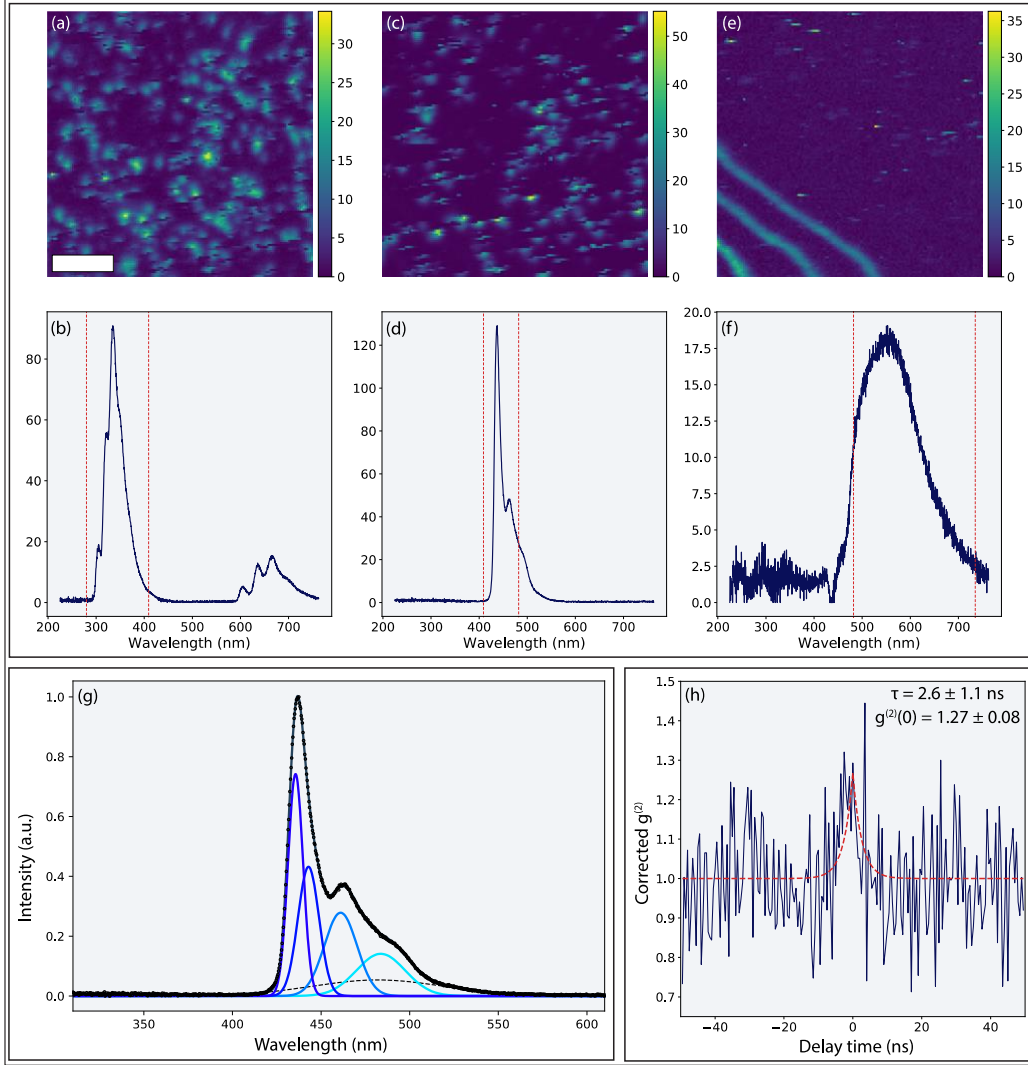


Figure 3: Hyperspectral characterization of a dense array of quantum emitters across three spectral regions in h-BN. Hyperspectral CL data were decomposed using Non-Negative Matrix Factorization (NMF) to display the main features of the data. Each image component (top row, scale bar 1 μm) shows the spatial distribution of the associated spectral component below (middle row). The red lines on the spectral components in panels (b), (d), and (f) show the edges of the bandpass filters used in bandpass imaging from figure (2). The first components in panels (a) and (b) shows point-like UV emitters from 300-400 nm. The peaks between 600-700 nm are artefacts due to the second-order reflections of the UV light from the spectrometer grating. Panels (c) and (d) show the spectral signature of the newly discovered blue quantum emitters between 400-500 nm. Panels (e) and (f) show that regions of the crystal with extended defects or strain give rise to emission between 500-700 nm. Panel (g) shows a rescaled view of the blue emission component as well as the results of multi-gaussian fitting of the peak. The fitted components show a Zero-Phonon Line (ZPL) followed by several phonon replicas with decreasing amplitude, an indicator of a single-photon emitter weakly coupled to the lattice. The photon-correlation curve in (h) shows a bunching peak, a signature of quantum emission in CL. Fitting to a single exponential decay model gives a lifetime of several nanoseconds, similar to lifetimes observed from SPE in other defects in h-BN.

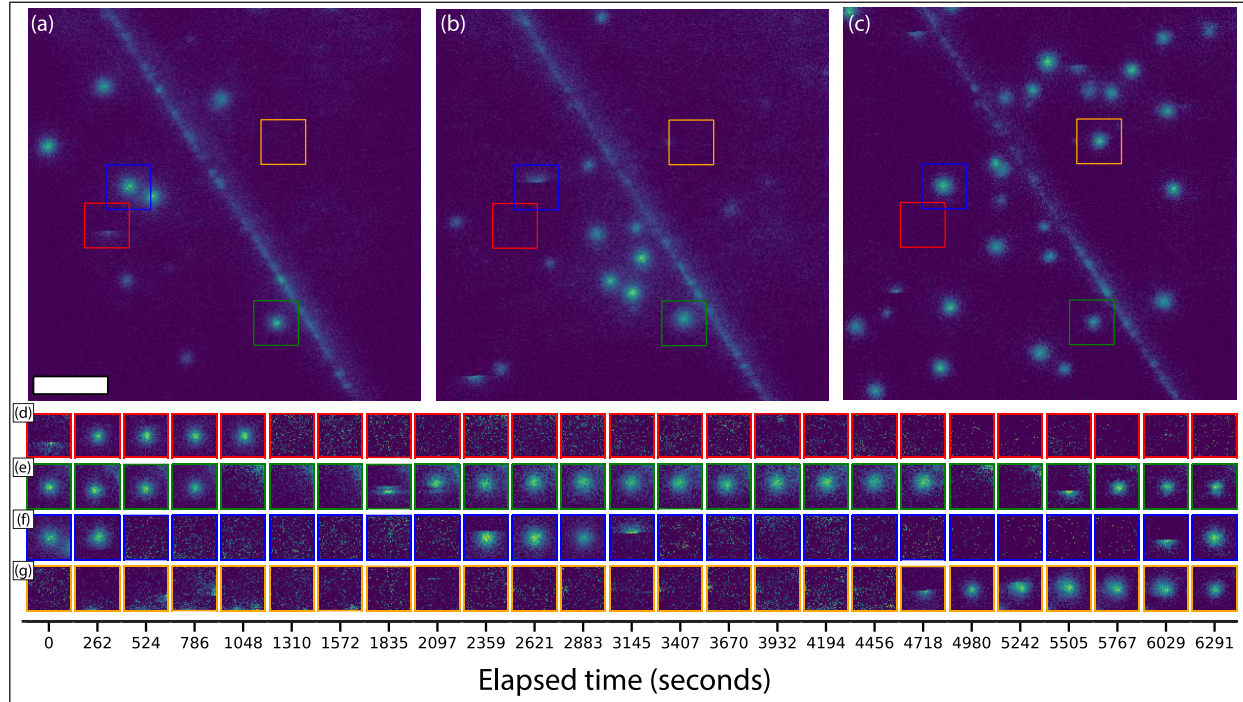


Figure 4: Overview of blinking behavior in hBN emitters. A series of CL bandpass images (409-482 nm) were taken over ~1.5 hours at ~4.5 minutes per image, with each frame corresponding to an electron beam dose of $2.3 \times 10^7 e^-/\text{\AA}^2$. The top row shows the first, middle, and final images in the series at full spatial resolution (scale bar is 500 nm). The bottom row shows the dynamic behavior of 4 separate 300 nm regions (indicated by the colored boxes in the top panel) over the entire time series. The emitters exhibit clear blinking behavior, turning on and off between frames of the time series. The electron beam clearly activates and deactivates the emitters, evidenced by those emitters that sharply turn on or off as the beam is passing over them.

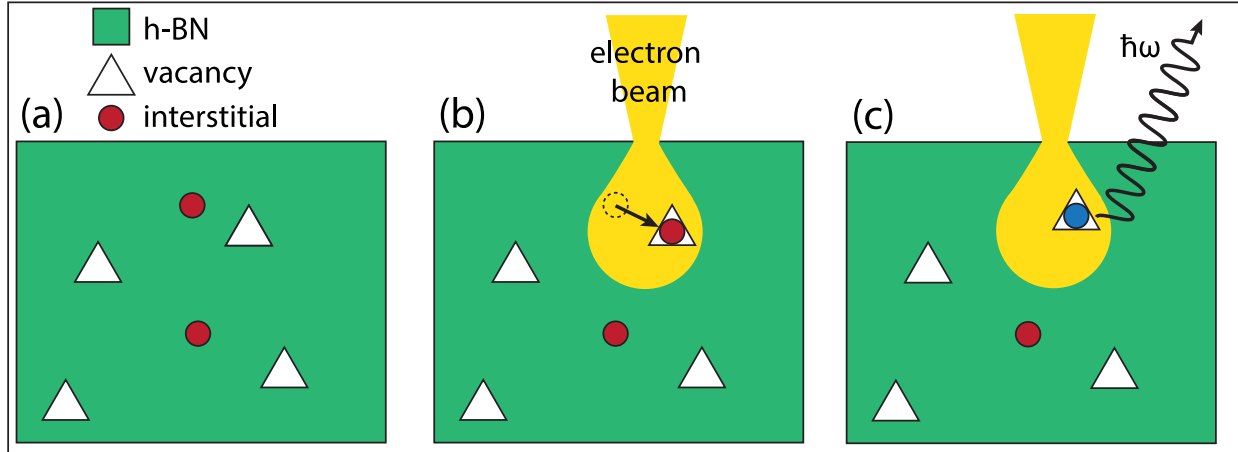


Figure 5: Proposed model for formation and activation of blue quantum emitters in NIMS-BN. The as-synthesized material has some intrinsic density of interstitial impurities and lattice vacancies, as shown in (a). When stimulated by the electron beam, the impurity atoms are driven into the vacancies and due to the energy provided by the beam a substitutional defect complex is formed. The charge state of the new defect is changed by the beam causing it to emit photons. The charge state of the defect is sensitive to the intense stimulus from the electron probe and can jump between emissive and non-emissive states, resulting in a blinking effect.